

Dynamic characteristics of terahertz hot-electron graphene FET bolometers: effect of electron cooling in channel and at side contacts

V. Ryzhii¹, C. Tang^{1,2}, T. Otsuji¹, M. Ryzhii³, V. Mitin⁴, and M. S. Shur⁵

¹Research Institute of Electrical Communication, Tohoku University, Sendai 980-8577,

Japan

²Frontier Research Institute for Interdisciplinary Sciences, Tohoku University, Sendai 980-8578,

Japan

³Department of Computer Science and Engineering, University of Aizu, Aizu-Wakamatsu 965-8580,

Japan

⁴Department of Electrical Engineering, University at Buffalo, SUNY, Buffalo, New York 14260,

USA

⁵Department of Electrical, Computer, and Systems Engineering,

Rensselaer Polytechnic Institute, Troy, New York 12180,

USA

We analyze the operation of the hot-electron FET bolometers with the graphene channels (GCs) and the gate barrier layers (BLs). Such bolometers use the thermionic emission of the hot electrons heated by incident modulated THz radiation. The hot electron transfer from the GC into the metal gate. As the THz detectors, these bolometers can operate at room temperature. We show that the response and ultimate modulation frequency of the GC-FET bolometers are determined by the efficiency of the hot-electron energy transfer to the lattice and the GC side contacts due to the 2DEG lateral thermal conductance. The dependences of these mechanisms on the band structure and geometrical parameters open the way for the GC-FET bolometers optimization, in particular, for the enhancement of the maximum modulation frequency.

I. INTRODUCTION

The specific band alignment in metal/black-P_xAs_{1-x} layer/graphene structures^{1,2} enables an enhanced thermionic electron and hole thermionic emission between the graphene and metal layers. Since the absorption of THz leads to an effective electron (holes) heating, the field-effect transistors (FETs) based on such structures with the metal gate (MG), b-P_xAs_{1-x} barrier layer (BL), and graphene channel (GC) can be used as sensitive bolometric detectors³⁻⁵. The responsivity of the GC-FET bolometers is determined by the rate of the carrier cooling due to the transfer of their energy to the GC and the side contacts (source and drain) as well as the thermionic emission⁴⁻⁷ (the Peltier cooling). On the other hand, the same processes determine the speed of the bolometric detectors in question. The roles of the effects in question depend on the structural parameters and the temperature. The plasmonic resonances in the gate GC of the devices under consideration can substantially affect the absorption of the impinging radiation and, hence, the detector performance. The recently proposed GC-FET bolometers with the composite BL^{8,9} have reinforced plasmonic resonances. Such a composite BL is made of the h-BN layer with a short narrow-gap black-P_xAs_{1-x} region. The latter serves as the electron emission window, through which the hot electrons pass from the GC into the MG. Since the quality of the h-BN/GC interface supports very high electron mobility (see, for example,^{10,11}) and, therefore, a low electron collision frequency, the plasmonic oscillations damping in the GC-FETs can be markedly weaker than in the GC-FETs with black-P_xAs_{1-x} BLs. Due to a relatively narrow emission window, the role of the Peltier cooling is diminished.

In this paper, we consider the GC-FETs with the n-type GC and composite h-BN/b-P BL and analyze the dynamics of the two-dimensional electron gas (2DEG) heating. We calculate

the GC-FET bolometer's modulation characteristics and the ultimate modulation frequency of the detected incoming radiation signals as functions of the device structure parameters and the temperature.

II. GC-FET DETECTOR STRUCTURE AND MAIN MODEL EQUATIONS

Figure 1(a) schematically shows the cross-section of the GC-FET structure under consideration. The GC-FET structure incorporates the GC separated from the MC by the composite h-BN/b-P/h-BN gate BL. For the GC-FETs with the Al MG, one can set for the differences between the bottom of the BL conduction band and the Dirac point in the GC $\Delta_C = 225$ meV, and the difference in the electron affinities of the Al MG and b-P in the central section of the gate BL $\Delta_M = 85$ meV¹²⁻¹⁸. We assume that the electron Fermi energy in the GC is chosen to satisfy the conditions: $\Delta_C - \mu = \Delta_M$. The lengths of the b-P central section and each the h-BN side sections are $2L_C$ and $L - L_C$, respectively [$2L_C < 2L$, see Fig. 1(a)]. Here $2L$ and $2L_C$ are the length of the GC and the length of the central GC section covered by the b-P section of the gate BL. Figs. 1(b) and 1(c) show the GC-FET band diagrams at the gate voltage V_G for different GC sections: in the side regions ($L_C < |x| < L$) and the central region ($|x| < L_C$). The current between the GC and MG in the side sections ($L_C < |x| < L$) is blocked because of the high-energy h-BN barrier. Since the energy barrier, Δ_C , for electrons in the GC in the section covered by the b-P is smaller than in the sections with the h-BN gate BL, this section plays the role of the electron emission window. The band diagram shown in Figs. 1(c) corresponds to the band parameter assumed above. For these conditions, the thermionic current from the GC into

the MC is associated with the electrons heated by the absorbed THz radiation in the whole GC flowing over the barrier via the central region.

The bias DC gate voltage V_G and the signal ac voltage, $\delta V_\omega^{0m} = \delta V_\omega \exp(-i\omega t)[1 + m \cos(\omega_m t)]$ are applied between the MG and the GC edge contacts. The signal voltage is produced by the energy flux, $I = I_\omega[1 + m \cos(\omega_m t)]$, of the impinging amplitude-modulated THz radiation (received by an antenna). Here ω is the THz radiation carrier frequency, $m = \delta I_\omega / I_\omega < 1$ and ω_m are the modulation depth and frequency ($\omega_m \ll \omega$). The absorption of the received amplitude-modulated THz radiation by the 2DEG leads to transient heating. As a result, the electron effective temperature averaged over the period of the carrier signal $2\pi/\omega$ (i.e., over the fast oscillations) is $\langle \bar{T} \rangle = T_0 + \langle \delta T_\omega \rangle + \langle \delta T_\omega^{0m} \rangle$, where T_0 is the lattice temperature, $\langle \delta T_\omega \rangle$ is the temperature variation associated with the heating caused by the carrier signal, and $\langle \delta T_\omega^{0m} \rangle$ is the slowly varying component associated with the modulation. The symbol $\langle \dots \rangle$ denotes the averaging over the fast oscillations with the characteristic period $2\pi/\omega_m \gg 2\pi/\omega$. The rectified DC and modulation components of the thermionic current via the b-P section, $\langle \delta J_\omega \rangle$ $\langle \delta J_\omega^{0m} \rangle$, can be presented as:

$$\langle \delta J_\omega \rangle = j^{max} HF \int_{-L_C}^{L_C} dx \frac{\langle \delta T_\omega \rangle}{T_0}, \quad (1)$$

$$\langle \delta J_\omega^{0m} \rangle = j^{max} HF \int_{-L_C}^{L_C} dx \frac{\langle \delta T_\omega^{0m} \rangle}{T_0}. \quad (2)$$

Here j^{max} is the maximal value of the current density from the GC, (the axis x is directed in the GC plane from one side contact to the other), H is the GC width (in the in-plane y -direction) and

$$F = \frac{\Delta_M}{T_0} \exp\left(-\frac{\Delta_M}{T_0}\right). \quad (3)$$

The exponential factor in the right-hand side of Eq. (3) has the activation energy for the electrons leaving the GC equal to $(\Delta_C - \mu)$. The maximal current density j^{max} is estimated as $j^{max} = e\Sigma/\tau_\perp$, where Σ and τ_\perp are the electron density in the GC (both associated with the doping and the gate bias voltage), the escape time of the electrons with the energy exceeding the barrier height, respectively, and e is the electron charge. Since the escape of an electron from the GC is associated with a significant change in its momentum, we set $\tau_\perp = \xi_\perp/v$, where v is the electron scattering frequency (inverse momentum relaxation time) in 2DEG at room temperature and $\xi_\perp \sim 1/2\pi$ is a phenomenological parameter (which for the virtually isotropic scattering of the electrons with the energy $\sim \Delta_C$ on acoustic phonons, can be roughly estimated as $1/2\pi$).

In the GC-FETs under consideration, the thermionic current of the heated electrons passes via the b-P region. Considering this, Eqs. (1) and (2) can be transformed to

$$\langle \delta J_\omega \rangle \simeq \frac{\langle \delta T_\omega \rangle|_{x=0}}{T_0}, \quad (4)$$

$$\langle \delta J_\omega^{0m} \rangle \simeq 2j^{max} L_C HF \frac{\langle \delta T_\omega^{0m} \rangle|_{x=0}}{T_0}. \quad (5)$$

The slow variations averaged over the fast oscillations (varying with the characteristic time $2\pi/\omega_m \gg 2\pi/\omega$) of the local electron temperature, $\langle \delta T_\omega^{0m} \rangle$, are governed by the following electron heat transport equation:

$$-h_e \frac{\partial^2 \langle \delta T_\omega^{0m} \rangle}{\partial x^2} + \frac{\langle \delta T_\omega^{0m} \rangle}{\tau_\epsilon} = \frac{\text{Re } \sigma_\omega \langle |\delta E_\omega|^2 \rangle}{\Sigma}, \quad (6)$$

$$\begin{aligned} c_e \frac{\partial \langle \delta T_\omega^{0m} \rangle}{\partial t} - h_e \frac{\partial^2 \langle \delta T_\omega^{0m} \rangle}{\partial x^2} + \frac{\langle \delta T_\omega^{0m} \rangle}{\tau_\epsilon} \\ = \frac{\text{Re } \sigma_\omega \langle |\delta E_\omega^{0m}|^2 \rangle}{\Sigma}. \end{aligned} \quad (7)$$

Here h_e and c_e are thermal conductivity and the electron thermal capacitance in the GC, τ_ϵ and τ_\perp are the electron energy relaxation time and the try-to-escape time for the electrons emitted via the BL central part, respectively, $v_W \simeq 10^8$ cm/s is the characteristic electron velocity in GCs, v is the electron scattering frequency, and $\sigma_\omega = [\sigma_0 v / (v - i\omega)]$, where $\sigma_0 = (e^2 \mu / \pi \hbar^2 v)$ is the 2DEG Drude conductivity, and δE_ω^{0m} is the ac electric field component in the GC corresponding to the modulated incoming THz radiation. The terms on the left sides of Eqs. (6) and (7), proportional to h_e and τ_ϵ^{-1} , describe the electron energy transfer to the side contacts due to the electron heat transport along the GC and to the phonon system (particularly to optical phonons). The contribution of the Peltier cooling is disregarded because of the small emission window ($L_C \ll L$). The term on the right-hand side of these equations describes the local power received by the 2DEG in the GC from the incident THz radiation (per an electron). Using the general formula for the degenerate 2DEG electron thermal capacitance^{19,20} and the expression for the GC density of states, one can obtain $c_e = (2\pi^2 T_0 / 3\mu)$. The quantity $h_e = v_W^2 / 2v$, which is in line with the Wiedemann-Franz relation^{21,22}.

Assuming low thermal resistance of the side contacts, the boundary conditions for Eq. (3) are set to be

$$\langle \delta T_\omega \rangle|_{x=\pm L} = 0, \quad \langle \delta T_\omega^{0m} \rangle|_{x=\pm L} = 0. \quad (8)$$

Accounting for the transformation of the THz signal receiving by an antenna to the AC electric field in the GC under the condition of the plasmonic oscillations excitation, one can obtain the following^{3,5,9} (see, also Refs. [23,24]):

$$\langle |\delta E_\omega|^2 \rangle = \frac{16}{g c} \left| \frac{\gamma_\omega \sin(\gamma_\omega x / L)}{\cos \gamma_\omega} \right|^2 I_\omega, \quad (9)$$

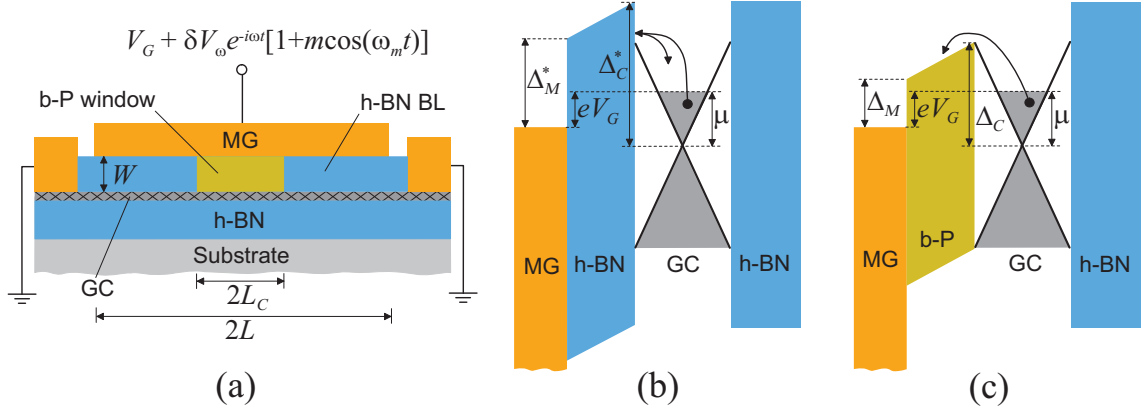


FIG. 1. (a) Cross-section of the GC-FET detector structure with composite BL and its band diagrams under the applied voltage gate voltage V_G in (b) the side regions ($L_C < |x| < L$) with a high barrier for electrons in GC reflecting them and (c) in the central region ($|x| < L_C$) with a moderately high barrier (see ^{8,9}).

$$\langle |\delta E_\omega^{\omega_m}|^2 \rangle = \frac{16}{g c} \left| \frac{\gamma_\omega \sin(\gamma_\omega x/L)}{\cos \gamma_\omega} \right|^2 \delta I_\omega \cos(\omega_m t). \quad (10)$$

Here $g \simeq 1.64$ is the antenna gain (for a half-wavelength dipole antenna), c is the speed of light in vacuum, $\gamma_\omega = \pi \sqrt{\omega(\omega + i\nu)}/2\Omega$ and $\Omega = (\pi e/\hbar L) \sqrt{\mu W/\kappa}$ are the effective wavenumber and the plasmonic frequency, respectively, with κ and W being the dielectric constant of the BL and its thickness.

Combining Eqs. (6), (7), (9), and (10), we arrive at

$$-h_e \frac{\partial^2 \langle \delta T_\omega \rangle}{\partial x^2} + \frac{\langle \delta T_\omega \rangle}{\tau_\epsilon} = \beta \frac{v_W^2}{L^2 \Omega^2} \left(\frac{\hbar v}{\mu} \right) \frac{\omega}{\sqrt{\omega^2 + v^2}} \left| \frac{\sin(\gamma_\omega x/L)}{\cos \gamma_\omega} \right|^2 I_\omega, \quad (11)$$

$$c_e \frac{\partial \langle \delta T_\omega^{\omega_m} \rangle}{\partial t} - h_e \frac{\partial^2 \langle \delta T_\omega^{\omega_m} \rangle}{\partial x^2} + \frac{\langle \delta T_\omega^{\omega_m} \rangle}{\tau_\epsilon} = \beta \frac{v_W^2}{L^2 \Omega^2} \left(\frac{\hbar v}{\mu} \right) \frac{\omega}{\sqrt{\omega^2 + v^2}} \left| \frac{\sin(\gamma_\omega x/L)}{\cos \gamma_\omega} \right|^2 \delta I_\omega \cos(\omega_m t), \quad (12)$$

where $\beta = \frac{4\pi^2}{137g} \simeq 0.176$ and θ is the phase shift. Here we have accounted for the fine structure constant $e^2/\hbar c = 1/137$.

III. OUTPUT RECTIFIED DC AND MODULATION CURRENTS

In the most interesting frequency range $\omega, \Omega \gg v$, the right-hand sides of Eqs. (11) and (12) can be somewhat simplified. This allows to obtain relatively simple and transparent expressions for $\langle \delta T_\omega^{\omega_m} \rangle$ and $\langle \delta T_\omega^{\omega_m} \rangle$ in closed analytic form. Such an approach was verified by the comparison of the results of the analytical and computer modeling. As shown in Sec. IV,

the results of the analytical and computer calculations are very close when $\omega, \Omega \gg v$.

Considering this and solving simplified versions of Eqs. (11) and (12) with the boundary conditions given by Eq. (8), at $\omega, \Omega \gg v$, we obtain the following formulas used for the derivation of GC-FET characteristics:

$$\langle \delta T_\omega \rangle|_{x=0} \propto \frac{1}{\mu} \left(\frac{v_W \tau_\epsilon}{v L^2} \right) \Pi_\omega r_\omega I_\omega, \quad (13)$$

$$\langle \delta T_\omega^{\omega_m} \rangle|_{x=0} \propto \frac{1}{\mu} \left(\frac{v_W \tau_\epsilon}{v L^2} \right) \frac{|\Pi_\omega^{\omega_m}| r_\omega \cos(\omega_m t + \theta)}{\sqrt{1 + (\omega_m/\bar{\omega}_m)^2}} \delta I_\omega. \quad (14)$$

Here

$$\Pi_\omega \simeq 1 - \frac{1}{1 + (\pi\omega/a\Omega)^2} - \left[1 - \frac{\cos(\pi\omega/\Omega)}{1 + (\pi\omega/a\Omega)^2} \right] \frac{1}{\cosh(a)}, \quad (15)$$

$$\Pi_\omega^{\omega_m} \simeq 1 - \frac{1}{1 + (\pi\omega/a_m\Omega)^2} - \left[1 - \frac{\cos(\pi\omega/\Omega)}{1 + (\pi\omega/a_m\Omega)^2} \right] \frac{1}{\cosh(a_m)}, \quad (16)$$

where the parameters $a_m = a \sqrt{1 - i\omega_m/\bar{\omega}_m}$, $a = L/\mathcal{L} = L \sqrt{2v/v_W^2 \tau_\epsilon}$ with $\mathcal{L} = \sqrt{\hbar e \tau_\epsilon}$, and $\bar{\omega}_m = 1/c_e \tau_\epsilon$ characterizing the 2DEG cooling at the side contacts,

$$r_\omega = [\sin^2(\pi\omega/2\Omega) + (4\Omega/\pi v)^2 \cos^2(\pi\omega/2\Omega)]^{-1} \quad (17)$$

is the factor describing the plasmonic resonances, and θ is a phase shift. The factor μ^{-1} in the right-hand sides of Eqs. (13) and (14) appears because the 2DEG conductivity and density are $\sigma_\omega \propto \sigma_0 \propto \mu$ and $\Sigma \propto \mu^2$, respectively, so that $\sigma_\omega/\Sigma \propto \mu^{-1}$. One needs to note that the Fermi energy μ is assumed to be fixed to provide a proper band alignment as stated above.

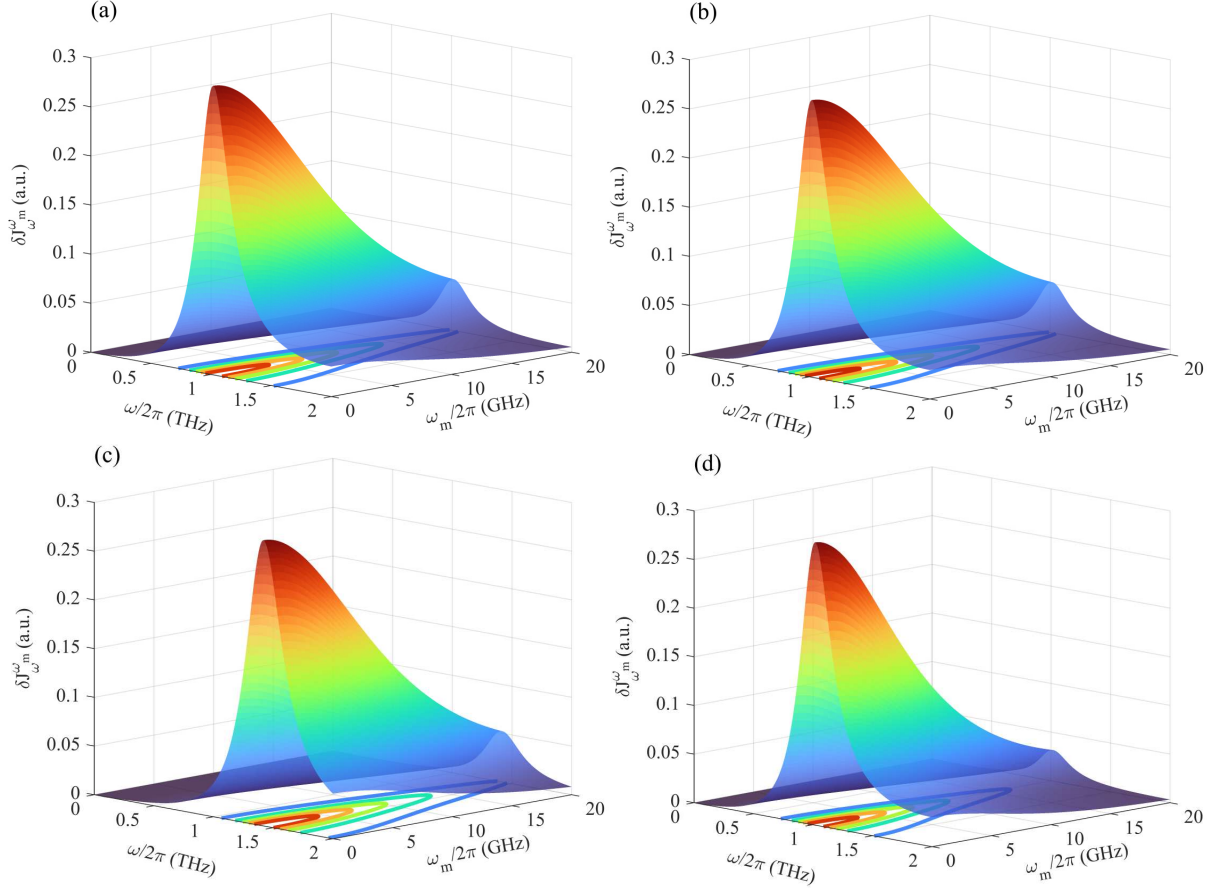


FIG. 2. Amplitude of modulated current $\langle \delta J_{\omega}^{\omega_m} \rangle$ as a function of signal frequency $\omega/2\pi$ and modulation frequencies $\omega_m/2\pi$: (a) $2L = 1.4 \mu\text{m}$, $\Omega/2\pi = 1.0 \text{ THz}$, $\nu = 0.5 \text{ ps}^{-1}$, and $\tau_e = 10 \text{ ps}$, (b) $2L = 1.0 \mu\text{m}$, $\Omega/2\pi = 1.4 \text{ THz}$, $\nu = 1.0 \text{ ps}^{-1}$, and $\tau_e = 10 \text{ ps}$, (c) $2L = 1.4 \mu\text{m}$, $\Omega/2\pi = 1.0 \text{ THz}$, $\nu = 1.0 \text{ ps}^{-1}$, (d) $2L = 1.4 \mu\text{m}$, $\Omega/2\pi = 1.0 \text{ THz}$, $\nu = 1.0 \text{ ps}^{-1}$, and $\tau_e = 12.5 \text{ ps}$.

Further, for the rectified dc current $\langle J_{\omega} \rangle$, the amplitude of the modulated current $\langle \delta J_{\omega}^{\omega_m} \rangle$, and for the pertinent current responsivities $\mathcal{R}_{\omega} = \langle J_{\omega} \rangle / I_{\omega}$ and $\mathcal{R}_{\omega}^{\omega_m} = \langle \delta J_{\omega}^{\omega_m} \rangle / \delta I_{\omega}$ we obtain using Eqs. (4), (5), (13), and (14):

$$R_{\omega} \propto \frac{2LCF}{\tau_{\perp}} \left(\frac{v_W^2 \tau_e}{vL^2} \right) r_{\omega} |\Pi_{\omega}|, \quad (18)$$

$$R_{\omega}^{\omega_m} \propto \frac{2LCF}{\tau_{\perp}} \left(\frac{v_W^2 \tau_e}{vL^2} \right) \frac{r_{\omega} |\Pi_{\omega}^{\omega_m}|}{\sqrt{1 + (\omega_m/\bar{\omega}_m)^2}}. \quad (19)$$

Accordingly, for the voltage responsivities we obtain

$$U_{\omega} = R_{\omega} \rho_L, \quad U_{\omega}^{\omega_m} = R_{\omega}^{\omega_m} \rho_L, \quad (20)$$

where $\rho_L \propto 1/LCF$ is the load resistance (in the GC/MG circuit).

Figure 2 shows the modulated current responsivity $\mathcal{R}_{\omega}^{\omega_m}$ (amplitude of modulated current $\langle \delta J_{\omega}^{\omega_m} \rangle$) versus the signal frequency $\omega/2\pi$ and modulation frequencies, $\omega/2\pi$ and $\omega_m/2\pi$, calculated using Eq. (19).

In this and the following figures we assume that $W = 10 \text{ nm}$, $\kappa = 4$, $\mu = 140 \text{ meV}$ (to fit the condition $\mu = \Delta_C - \Delta_M$, where for Al MG $\Delta_C = 225 \text{ meV}$ and $\Delta_M = 85 \text{ meV}$), $\tau_e = 5 - 15 \text{ ps}$, $\nu = 0.5 - 1.5 \text{ ps}^{-1}$, and $T_0 = 25 \text{ meV}$, so that $c_e = 1.175$ ($\bar{\omega}_m/2\pi \simeq 9 - 27 \text{ GHz}$). The chosen values of τ_e generally correspond to the electron energy relaxation in GCs primarily on optical phonons²⁵⁻²⁹. As seen in Fig. 2, the amplitude of the modulated current exhibits maxima associated with the fundamental plasmonic resonances $\omega \simeq \Omega$. When the signal frequency ω tends to zero, the modulation current $\delta J_{\omega}^{\omega_m}$ (as well as δJ_{ω}) also approaches zero. This is because of the heating electric field along the GC δE_{ω} vanishes in line with Eqs. (9) and (10). According to the plots in Fig. 2, the position of resonant peak shifts with changing GC length $2L$ according to $\Omega \propto L^{-1}$ [compare Figs. 2(a) and 2(b)]. Comparing Figs. 2(c) and 2(d), one can see that the variation of the electron energy relaxation time τ_e leads first to higher values of $\delta J_{\omega}^{\omega_m}$ at low modulation frequencies $\omega_m/2\pi$ and to a faster decrease in $\delta J_{\omega}^{\omega_m}$ at higher $\omega_m/2\pi$. A lowering of the resonant maxima with rising modulation frequency ω_m is attributed to the weakening of the 2DEG heating when $(\omega_m/\bar{\omega}_m)$ increases

Figures. 3 and 4 show the dependencies of the modulated current peak values $\langle \delta J_{\Omega}^{\omega_m} \rangle \propto R_{\Omega}^{\omega_m}$ on the electron collision

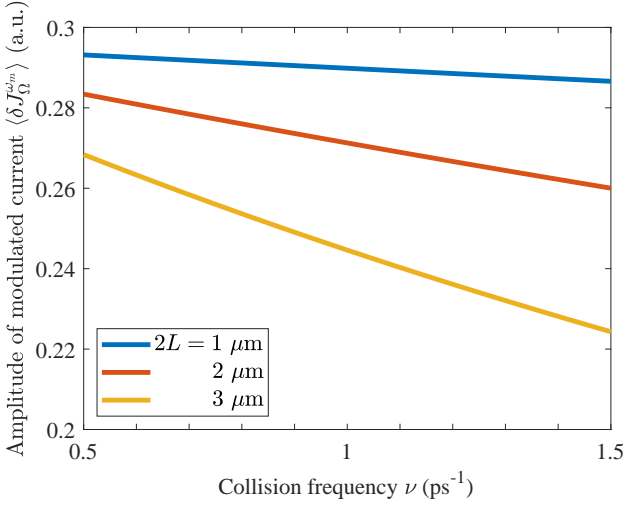


FIG. 3. Amplitude of modulated current $\langle \delta J_{\omega}^{\omega_m} \rangle$ as a function of the electron collision frequency ν for different GC length $2L$ ($\tau_{\epsilon} = 10$ ps, $\omega_m/2\pi = 13.5$ GHz).

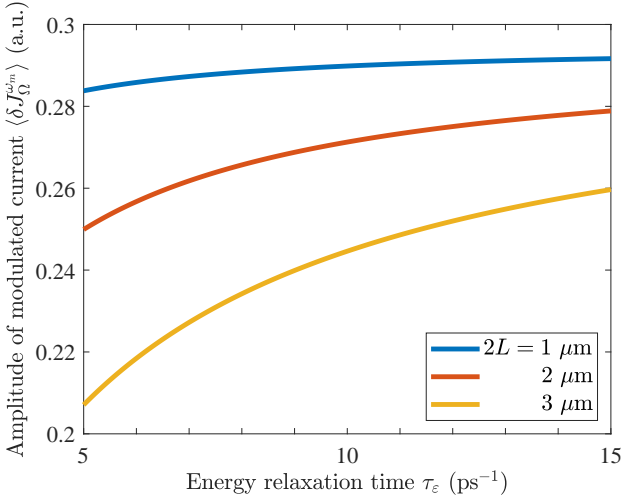


FIG. 4. Amplitude of modulated current $\langle \delta J_{\omega}^{\omega_m} \rangle$ as a function of the electron energy relaxation time τ_{ϵ} for different GC length $2L$ ($\nu = 1.0$ ps⁻¹, $\omega_m/2\pi = 13.5$ GHz).

frequency ν (at fixed electron energy relaxation time τ_{ϵ}) and on τ_{ϵ} (at fixed ν) calculated for different GC length $2L$. To maintain $\Omega/2\pi = 1.0$ THz for different L , the curves of Figs. 3 and 4 correspond to different values of the BL W thickness ($\Omega \propto \sqrt{W}/L = \text{const}$).

IV. MODULATION CHARACTERISTIC

Introducing the detector modulation efficiency

$$M_{\omega}^{\omega_m} = \frac{R_{\omega}^{\omega_m}}{R_{\omega}} = \frac{U_{\omega}^{\omega_m}}{U_{\omega}} \quad (21)$$

and accounting for Eqs. (18) and (19), for the fundamental plasmonic resonance ($\omega = \Omega$) we obtain

$$M_{\Omega}^{\omega_m} = \frac{1}{\sqrt{1 + (\omega_m/\bar{\omega}_m)^2}} \left| \frac{\Pi_{\Omega}^{\omega_m}}{\Pi_{\Omega}} \right|, \quad (22)$$

i.e., accounting for Eqs. (15) - (17),

$$M_{\Omega}^{\omega_m} = \frac{1}{\sqrt{1 + (\omega_m/\bar{\omega}_m)^2}} \times \left| \frac{1 - \frac{1}{1 + (\pi/a_m)^2} - \left[1 + \frac{1}{1 + (\pi/a_m)^2} \right] \frac{1}{\cosh(a_m)}}{1 - \frac{1}{1 + (\pi/a)^2} - \left[1 + \frac{1}{1 + (\pi/a)^2} \right] \frac{1}{\cosh(a)}} \right|. \quad (23)$$

Figure 5 shows the modulation efficiency $M_{\Omega}^{\omega_m}$ versus modulation frequency $\omega_m/2\pi$ for detectors with different GC lengths $2L$ and different values of scattering frequency ν in the main part of the CC (i.e., covered by the h-BN) at the plasmonic resonance $\omega = \Omega$. The dashed lines correspond to the first factor in the right-hand sides of Eqs. (22) and (23) $\bar{M}_{\Omega}^{\omega_m} = 1/\sqrt{1 + (\omega_m/\bar{\omega}_m)^2}$. This factor describes the net efficiency $M_{\Omega}^{\omega_m}$ roll-off with increasing modulation frequency ω_m associated solely with the 2DES cooling due to the electron energy relaxation in the GC. The inset on Figs. 5 shows the dependence of the second factor in Eqs. (22) and (23), i.e., $\Theta_m = \Pi_{\omega}^{\omega_m}/\Pi_{\omega}$ on $2L$ and ν . The factor Θ_m reflects the effect of the 2DEG cooling due to the electron heat transfer to the side contacts with the absorption of the electron's excessive thermal energy by these contacts (the heat transfer factor). As seen from Fig. 5, the modulation efficiency $M_{\Omega}^{\omega_m}$ is markedly larger than $\bar{M}_{\Omega}^{\omega_m}$ (compare the solid and dashed lines). This is attributed to the fact that Θ_m is larger than unity as shown in the inset. In the latter case the maximal modulation frequency ω_m^{max} defined by the relation $M_{\Omega}^{\omega_m^{\text{max}}} = 1/\sqrt{2}$ exceeds $\bar{\omega}_m$.

Figures. 6 and 7 show the maximal modulation frequency $\omega_m^{\text{max}}/2\pi$. The red curves in Figs. 6 and 7 correspond to the same set of parameters.

As follows from Figs. 5 - 7, the maximal modulation frequency $\omega_m^{\text{max}}/2\pi$ in the GC-FET detectors with the GC length $2L = (1 - 3) \mu\text{m}$ can be about dozens GHz.

V. COMPARISON OF MODULATION CHARACTERISTICS OF GC-FETS WITH COMPOSITE AND UNIFORM BLS

The characteristics of GC-FETs with the uniform BL can be obtained from Eqs. (1), (2), (11), and (12) setting $L_C = L$. In this case, the electron collision frequency ν and the factors Π_{ω} and $\Pi_{\omega}^{\omega_m}$ should be replaced by $\tilde{\nu}$, $\tilde{\Pi}_{\omega}$, and $\tilde{\Pi}_{\omega}^{\omega_m}$, respectively. The electron collision frequency in the GC encapsulated in h-BN ν is usually smaller than that in the case of the GC sandwiched between the h-BN substrate and the b-p BL $\tilde{\nu}^{30}$. The consideration of the intermediate case $L_C \lesssim L$

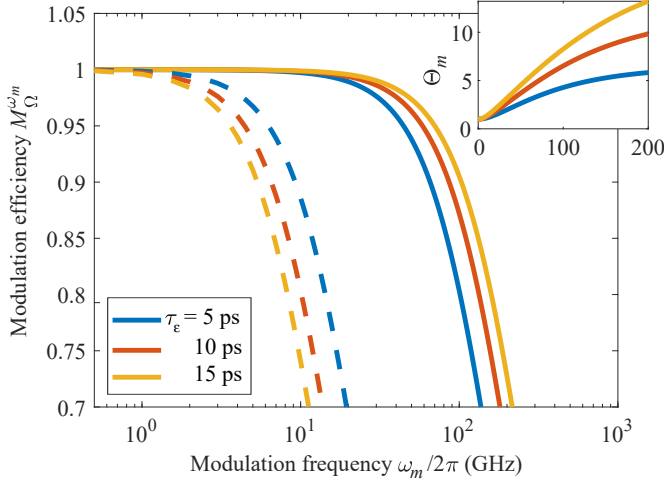


FIG. 5. Modulation efficiency $M_{\Omega}^{\omega_m}$ at the plasmonic resonance ($\omega = \Omega$) versus the modulation frequency $\omega_m/2\pi$ for different values of electron energy relaxation time τ_{ϵ} ($2L = 2.0 \mu\text{m}$, $\nu = 1.0 \text{ ps}^{-1}$). The dashed lines and the inset correspond to $\bar{M}_{\Omega}^{\omega_m}$ and Θ_m versus $\omega_m/2\pi$ dependences.

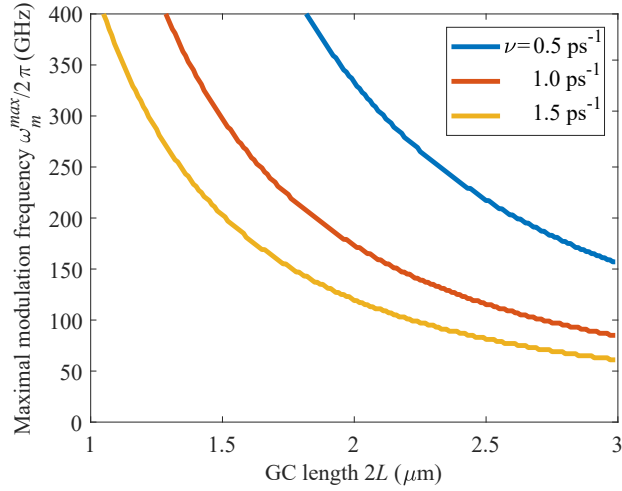


FIG. 6. Maximal modulation frequency $\omega_m^{\text{max}}/2\pi$ versus GC length $2L$ for different values of collision frequency ν and $\tau_{\epsilon} = 10 \text{ ps}$.

leads to rather cumbersome formulas and, therefore, will not be studied below.

Comparing the modulated current responsivities, $\mathcal{R}_{\Omega}^{\omega_m}$ and $\bar{\mathcal{R}}_{\Omega}^{\omega_m}$, and the modulation efficiencies, $M_{\Omega}^{\omega_m}$ and $\bar{M}_{\Omega}^{\omega_m}$, of the GC-FET bolometric detectors with that of the composite h-BN/b-P BL given by Eqs. (19) and (23) and those of the detectors with the uniform b-P BL (which are derived using⁹) at the plasmonic resonance, we obtain

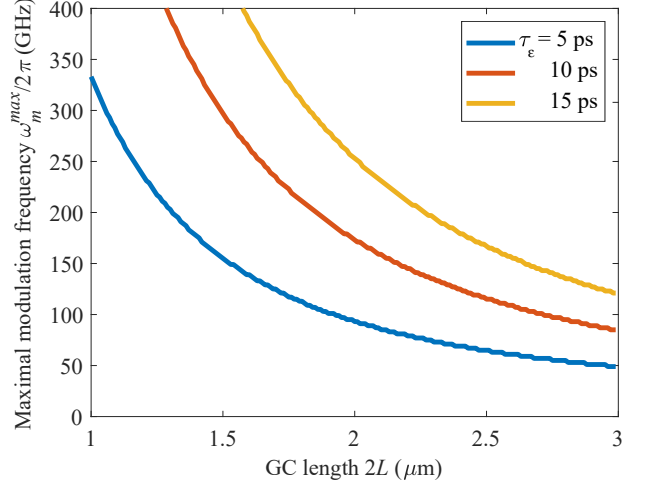


FIG. 7. The same dependences as in Fig. 6, but for different values of electron energy relaxation time τ_{ϵ} ($\nu = 1.0 \text{ ps}^{-1}$).

$$\mathcal{R}_{\omega}^{\omega_m} = \frac{R_{\omega}^{\omega_m}}{\bar{R}_{\omega}^{\omega_m}} = \frac{L_C \tilde{\nu}}{L \nu} \times \left| \frac{1 - \frac{1}{1 + (\pi/a_m)^2} - \left[1 + \frac{1}{1 + (\pi/a_m)^2}\right] \frac{1}{\cosh(a_m)}}{1 - \left[1 + \frac{1}{1 + (\pi/\tilde{a}_m)^2}\right] \frac{\tanh(\tilde{a}_m)}{\tilde{a}_m}} \right| \quad (24)$$

and

$$\frac{M_{\Omega}^{\omega_m}}{\bar{M}_{\Omega}^{\omega_m}} = \left| \frac{1 - \left[1 + \frac{1}{1 + (\pi/\tilde{a})^2}\right] \frac{\tanh(\tilde{a})}{\tilde{a}}}{1 - \left[1 + \frac{1}{1 + (\pi/\tilde{a}_m)^2}\right] \frac{\tanh(\tilde{a}_m)}{\tilde{a}_m}} \right| \times \left| \frac{1 - \frac{1}{1 + (\pi/a_m)^2} - \left[1 + \frac{1}{1 + (\pi/a_m)^2}\right] \frac{1}{\cosh(a_m)}}{1 - \frac{1}{1 + (\pi/a)^2} - \left[1 + \frac{1}{1 + (\pi/a)^2}\right] \frac{1}{\cosh(a)}} \right|, \quad (25)$$

respectively. Here $\tilde{a} = L\sqrt{2\tilde{\nu}/v_W^2\tau_{\epsilon}}$, $\tilde{a}_m = \tilde{a}\sqrt{1 - i\omega_m/\bar{\omega}_m}$, hence $\tilde{a}/a = \tilde{a}_m/a_m = \sqrt{\tilde{\nu}/\nu}$ providing that the GCs of both types have the same length $2L$ and the electron energy relaxation time τ_{ϵ} , but different electron scattering frequencies ν and $\tilde{\nu}$.

If the load resistance is chosen to be equal to the GC/MG resistance, i.e., inversely proportion to $L_C F$,

$$\mathcal{U}_{\Omega}^{\omega_m} = \frac{U_{\Omega}^{\omega_m}}{\tilde{U}_{\Omega}^{\omega_m}} = \frac{L}{L_C} \frac{R_{\omega}^{\omega_m}}{\bar{R}_{\omega}^{\omega_m}} \propto \frac{\tilde{\nu}}{\nu}. \quad (26)$$

The latter ratio is independent of L_C .

Figs. 8 and 9 show the results of the comparison of the voltage responsivities of the GC-FET detectors with the composite h-BN/b-P/h-BN gate BL and with the uniform b-P gate

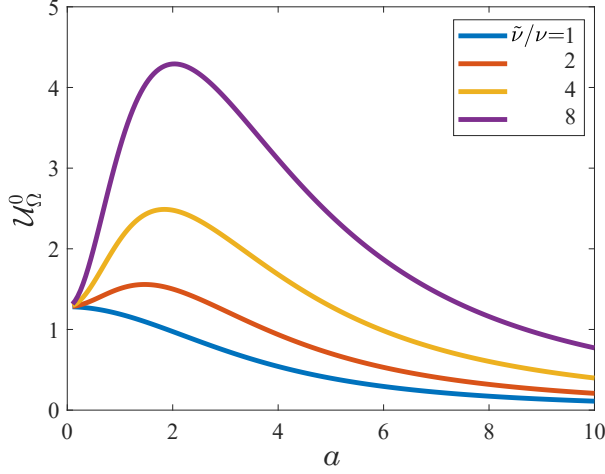


FIG. 8. Ratio of modulation voltage responsivities \mathcal{U}_Ω^0 at low modulation frequencies and plasmonic resonance ($\omega_m \ll \omega_m^{max}$ and $\omega = \Omega$) as a function of parameter $a = L/\mathcal{L} = L\sqrt{2v/v_W^2}\tau_e$ for different ratios and $\tilde{\nu}/\nu = (1-8)$.

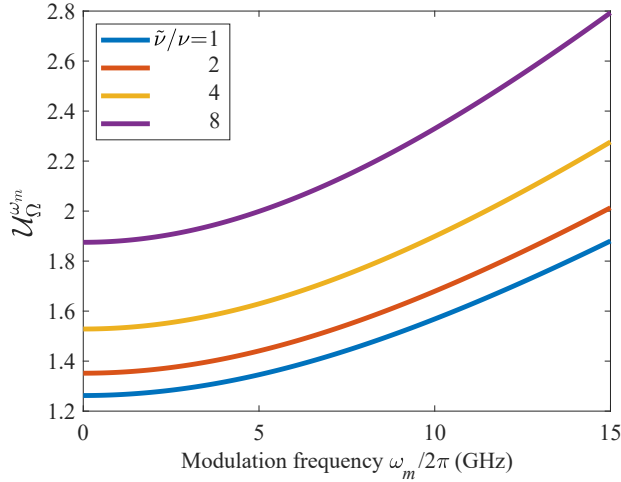


FIG. 9. Frequency dependences of the voltage responsivities ratio, $\mathcal{U}_\Omega^{\omega_m}$, for the GC-FET with the composite gate BL (and different $\tilde{\nu}$) and the GC-FETs with uniform gate: $v = 1.0 \text{ ps}^{-1}$ $L = 1 \text{ }\mu\text{m}$ and $\tau_e = 10 \text{ ps}$.

BL. One can see that the responsivity of the former exceeds that of the latter when $v < \tilde{\nu}$, which corresponds to the reality. This confirms the advantage of using the composite gate BL in the GC-FET bolometric detectors under consideration.

VI. COMPARISON OF COMPUTER AND ANALYTICAL MODELING: VERIFICATION OF ANALYTICAL MODEL

To verify the accuracy of the analytical results we compare the values of the normalized electron temperatures,

$\langle \delta\Theta_\omega \rangle^{comput}$ and $\langle \delta\Theta_\omega \rangle^{analyt}$, obtained from the differential Eq. (11) and using the analytical formula. These values are defined as

$$\langle \delta\Theta_\omega \rangle^{comput} = \langle \delta T_\omega \rangle^{comput} / \left(\frac{32\beta\hbar}{\pi^2\mu} I_\omega \right),$$

$$\langle \delta\Theta_\omega \rangle^{analyt} = \langle \delta T_\omega \rangle^{analyt} / \left(\frac{32\beta\hbar}{\pi^2\mu} I_\omega \right).$$

As a result, we arrive at the following dimensionless equations, respectively:

$$-\frac{\partial^2 \langle \delta\Theta_\omega \rangle^{comput}}{\partial \xi^2} + a^2 \langle \delta\Theta_\omega \rangle^{comput} = \left(\frac{\pi v}{4\Omega} \right)^2 \frac{\omega}{\sqrt{\omega^2 + v^2}} \times \left| \frac{\sin(\gamma_\omega \xi)}{\cos \gamma_\omega} \right|^2 \quad (27)$$

$$\langle \delta\Theta_\omega \rangle^{analyt} = \frac{r\omega}{2a^2} \times \left\{ 1 - \frac{\cos(\pi\omega x/\Omega L)}{1 + (\pi\omega x/\Omega)^2} - \left[1 - \frac{\cos(\pi\omega/\Omega)}{1 + (\pi\omega/a\Omega)^2} \right] \frac{\cosh(ax/L)}{\cosh(a)} \right\} \quad (28)$$

Here $\xi = x/L$, so that the boundary conditions are $\langle \delta\Theta_\omega \rangle^{comput}|_{\xi=\pm 1} = \langle \delta\Theta_\omega \rangle^{analyt}|_{\xi=\pm 1} = 0$, and the factor $r\omega$ given by Eq (17).

All equations in this work were numerically calculated with MATLAB (version 9.14.0 R2023a, Natick, Massachusetts: The MathWorks Inc.). Finding the maximal modulation frequency ω_m^{max} (Figs. 6 and 7), we used the Parallel Computing Toolbox (*parfor*) to speed up massive calculations. The differential Eq. (27) was solved with a standard MATLAB function *dsolve*.

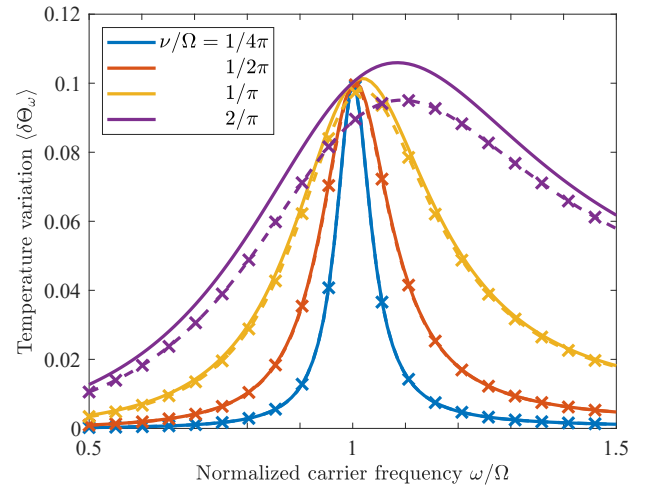


FIG. 10. Frequency dependences of the normalized temperature variations $\langle \delta\Theta_\omega \rangle|_{x=0}$ in the structure center obtained using computer (dashed lines with markers) and analytical (solid lines) modeling for different values of v/Ω and $a = 1$.

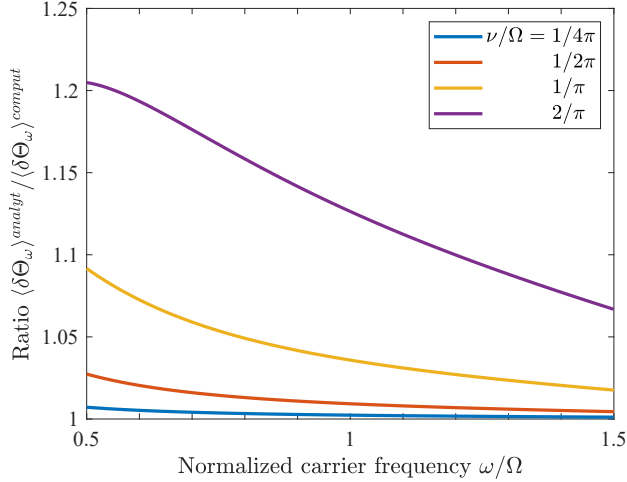


FIG. 11. Ratios of the normalized temperature variations $\langle \delta\Theta_\omega^{analyt} \rangle_{x=0}$ and $\langle \delta\Theta_\omega^{comput} \rangle_{x=0}$ in the structure center as functions of normalized carrier frequency ω/Ω obtained for different values of ν/Ω and $a = 1$.

Figure 10 shows that at low ratios of ν/Ω ($\nu/\Omega \leq 1/\pi$), the computer and analytical calculations provide practically distinguishable dependences. However, at a relatively large values of ν/Ω (of $\nu/\Omega = 2/\pi$), the distinction is visible reaching about 15%. This is confirmed also by the plots in Fig. 11.

Similar conclusion can be made in respect of the results following from Eqs. (12) and (14) (with the substitution of parameter a by a_m).

Thus, the above comparison of the results of the computer and analytical models justifies using Eqs. (13) and (14), which provide the GC-FET characteristics with sufficiently high accuracy.

VII. COMMENTS

The GC-FET detectors with a larger $2L$ exhibit smaller modulation currents $|\delta J_\Omega^{\omega_m}|$ (see Figs. 3 and 4). This is because at the same intensity of the impinging radiation, the amplitude of the signal electric field in the GC $|\delta E_\omega|$ decreases with increasing L resulting in a weaker electron heating. As seen from Eqs. (15) and (16), $\langle \delta T_\omega \rangle \propto \langle \delta T_\omega^{\omega_m} \rangle \propto L^{-2}$. However, an increase in $2L$ leads to a diminishing of the electron energy transfer to the side contact. The trade-off of such factors, gives rise to a relatively weak dependence of the modulation current of the GC length. This, in particular, follows from the comparison of $\langle \delta J_\Omega^{\omega_m} \rangle$ at $2L = 1 \mu\text{m}$ and $2L = 3 \mu\text{m}$ shown in Figs. 3 and 4.

Above, calculating the GC-FET characteristics, we assumed the room temperature operation. Lowering the working temperature might lead to a marked change of the GC-FETs performance as bolometric detectors. At lower the lattice temperatures T_0 , ν , and F decrease, while τ_ϵ simultaneously becomes larger. In particular, at not too low temperatures, the electron energy relaxation time and the electron scattering fre-

quency are determined by optical phonons^{27,28} and acoustic phonons^{31,32}, respectively, with $\tau_\epsilon \propto (T_0/\hbar\omega_0)^2 \exp(\hbar\omega_0/T_0)$ and $\nu \propto T_0$. Here $\hbar\omega_0 \simeq 200$ meV is the optical phonon energy. This implies that the characteristics obtained above might be substantially modified for GC-FET detectors operating at low temperatures. The latter is beyond the scope of this paper and requires a separate study.

VIII. CONCLUSION

We evaluated the performance of the hot-electron GC-FET bolometers with graphene channel and the composite h-BN/b-P/h-BN gate BL and showed that these bolometers can exhibit high values of the responsivity to the THz radiation modulated by signals of dozens GHz at room temperature. The predicted high performance of the GC-bolometers might encourage the fabrication of these devices and their characterization.

- ¹Y. Cai, G. Zhang, and Y. W. Zhang, "Layer-dependent band alignment and work function of few-layer phosphorene," *Sci. Rep.*, vol. 4, 6677, Oct. 20, 2014.
- ²X. Ling, H. Wang, S. Huang, F. Xia, and M. S. Dresselhaus, "The renaissance of black phosphorus," *PNAS*, vol. 112, no. 15, pp. 4523–4530, 2015.
- ³V. Ryzhii, C. Tang, T. Otsuji, M. Ryzhii, V. Mitin, and M. S. Shur, "Resonant plasmonic detection of terahertz radiation in field-effect transistors with the graphene channel and the black-As_xP_{1-x} gate layer," *Sci. Rep.*, vol. 13, no. 1, 2023.
- ⁴V. Ryzhii, C. Tang, T. Otsuji, M. Ryzhii, V. Mitin, and M. S. Shur, "Effect of electron thermal conductivity on resonant plasmonic detection in terahertz hot-electron bolometers based on metal/black-AsP/graphene FETs," *Phys. Rev. Appl.*, vol. 19, no. 6, 064033, 2023.
- ⁵V. Ryzhii, C. Tang, T. Otsuji, M. Ryzhii, V. Mitin, and M. S. Shur, "Hot-electron resonant terahertz bolometric detection in the graphene/black-AsP field-effect transistors with a floating gate," *J. Appl. Phys.*, vol. 133, no. 17, 174501, 2023.
- ⁶J. F. Rodríguez-Nieva, M. S. Dresselhaus, and L. S. Levitov, "Thermionic emission and negative dI/dV in photoactive graphene heterostructures," *Nano Lett.*, vol. 15, no. 3, pp. 1451–1456, 2015.
- ⁷J. F. Rodríguez-Nieva, M. S. Dresselhaus, and J. C. Song, "Enhanced thermionic-dominated photoresponse in graphene Schottky junctions," *Nano Lett.*, vol. 16, no. 10, pp. 6036–6041, 2016.
- ⁸M. Ryzhii, V. Ryzhii, T. Otsuji, C. Tang, V. Mitin, and S. Shur, "Resonant terahertz bolometric detectors using plasmonic response in graphene-channel FETs with b-P/h-BN gate barrier layers," in *The Int. IEEE Conf. on Microwaves, Communications, Antennas and Electronic Systems (IEEE COMCAS 2023)*, Tel-Aviv, Israel (accepted).
- ⁹M. Ryzhii, V. Ryzhii, M. S. Shur, V. Mitin, C. Tang, and T. Otsuji, "Terahertz bolometric detectors based on graphene field-effect transistors with the composite h-BN/black-P/h-BN gate layers using plasmonic resonances," *J. Appl. Phys.*, vol. 134, no. 8, 084501, 2023.
- ¹⁰A. S. Mayorov *et al.*, "Micrometer-scale ballistic transport in encapsulated graphene at room temperature," *Nano Lett.*, vol. 11, no. 6, pp. 2396–2399, 2011.
- ¹¹M. Yankowitz, Q. Ma, P. Jarillo-Herrero, and B. J. LeRoy, "van der Waals heterostructures combining graphene and hexagonal boron nitride," *Nat. Rev. Phys.*, vol. 1, no. 2, pp. 112–125, 2019.
- ¹²M. Uda, A. Nakamura, T. Yamamoto, and Y. Fujimoto, "Work function of polycrystalline Ag, Au and Al," *J. Electron. Spectrosc. Relat. Phenom.*, vol. 88, pp. 643–648, 1998.
- ¹³S. M. Song, J. K. Park, O. J. Sul, and B. J. Cho, "Determination of work function of graphene under a metal electrode and its role in contact resistance," *Nano Lett.*, vol. 12, no. 8, pp. 3887–3892, 2012.
- ¹⁴F. Liu, X. Zhang, P. Gong, T. Wang, K. Yao, S. Zhu, and Yan Lu, "Potential outstanding physical properties of novel black arsenic phosphorus As_{0.25}P_{0.75}/As_{0.75}P_{0.25} phases: a first-principles investigation," *RSC Adv.*, vol. 12, no. 6, pp. 3745–3754, 2022.

- ¹⁵T. Hu, B. Xu, and J. Hong, "Two-dimensional $As_{1-x}P_x$ binary compounds: Highly tunable electronic structure and optical properties," *Curr. Appl. Phys.*, vol. 17, no. 2, pp. 186–191, 2017.
- ¹⁶M. Xie *et al.*, "A promising two-dimensional solar cell donor: Black arsenic–phosphorus monolayer with 1.54 eV direct bandgap and mobility exceeding $14,000 \text{ cm}^2/\text{V}^{-1}\text{s}^{-1}$," *Nano Energy*, vol. 28, pp. 433–439, 2016.
- ¹⁷E. P. Young *et al.*, "Wafer-scale black arsenic–phosphorus thin-film synthesis validated with density functional perturbation theory predictions," *ACS Appl. Nano Mater.*, vol. 1, no. 9, pp. 4737–4745, 2018.
- ¹⁸B. Liu *et al.*, "Black arsenic-phosphorus: Layered anisotropic infrared semiconductors with highly tunable compositions and properties," *Adv. Mater.*, vol. 27, no. 30, pp. 4423–4429, 2015.
- ¹⁹Q. Li, X. Xie, and S. D. Sarma, "Calculated heat capacity and magnetization of two-dimensional electron systems," *Phys. Rev. B*, vol. 40, no. 2, pp. 1381–1384, 1989.
- ²⁰M. Massicotte, G. Soavi, A. Principi, and K.-J. Tielrooij, "Hot carriers in graphene—fundamentals and applications," *Nanoscale*, vol. 13, no. 18, pp. 8376–8411, 2021.
- ²¹Z. Tong, A. Pecchia, C. Yam, T. Dumitrică, and T. Frauenheim, "Ultra-high electron thermal conductivity in T-Graphene, Biphenylene, and Net-Graphene," *Adv. Energy Mater.*, vol. 12, no. 28, 2200657, 2022.
- ²²T. Y. Kim, C.-H. Park, and N. Marzari, "The electronic thermal conductivity of graphene," *Nano Lett.*, vol. 16, no. 4, pp. 2439–2443, 2016.
- ²³V. Ryzhii, A. Satou, and T. Otsuji, "Plasma waves in two-dimensional electron-hole system in gated graphene heterostructures," *J. Appl. Phys.*, vol. 101, no. 2, 024509, 2007.
- ²⁴V. Ryzhii, T. Otsuji, and M. Shur, "Graphene based plasma-wave devices for terahertz applications," *Appl. Phys. Lett.*, vol. 116, no. 14, 140501, 2020.
- ²⁵J. H. Strait, H. Wang, S. Shivaraman, V. Shields, M. Spencer, and F. Rana, "Very slow cooling dynamics of photoexcited carriers in graphene observed by optical-pump terahertz-probe spectroscopy," *Nano Lett.*, vol. 11, no. 11, pp. 4902–4906, 2011.
- ²⁶V. Ryzhii, M. Ryzhii, V. Mitin, A. Satou, and T. Otsuji, "Effect of heating and cooling of photogenerated electron–hole plasma in optically pumped graphene on population inversion," *Jpn. J. Appl. Phys.*, vol. 50, no. 9R, 094001, 2011.
- ²⁷V. Ryzhii *et al.*, "Graphene terahertz uncooled bolometers," *J. Phys. D: Appl. Phys.*, vol. 46, no. 6, 065102, 2013.
- ²⁸V. Ryzhii *et al.*, "Graphene vertical hot-electron terahertz detectors," *J. Appl. Phys.*, vol. 116, no. 11, 114504, 2014.
- ²⁹K. Tamura *et al.*, "Fast and sensitive terahertz detection with a current-driven epitaxial-graphene asymmetric dual-grating-gate field-effect transistor structure," *APL Photonics*, vol. 7, no. 12, 126101, 2022.
- ³⁰Y. Liu *et al.*, "Phonon-mediated colossal magnetoresistance in graphene/black phosphorus heterostructures," *Nano Lett.*, vol. 18, no. 6, pp. 3377–3383, 2018.
- ³¹F. Vasko and V. Ryzhii, "Voltage and temperature dependencies of conductivity in gated graphene," *Phys. Rev. B*, vol. 76, no. 23, 233404, 2007.
- ³²E. Hwang and S. D. Sarma, "Acoustic phonon scattering limited carrier mobility in two-dimensional extrinsic graphene," *Phys. Rev. B*, vol. 77, no. 11, 115449, 2008.